Geophysical Journal International

Geophys. J. Int. (2016) **204,** 1721–1728 doi: 10.1093/gji/ggv550

GJI Mineral physics, rheology, heat flow and volcanology

Dynamic elastic moduli during isotropic densification of initially granular media

Jérémie Vasseur,[1] Fabian B. Wadsworth,[1] Yan Lavallée[2] and Donald B. Dingwell[1]

[1] *Earth and Environmental Sciences, Ludwig Maximilian University, Munich, Germany. E-mail: jeremie.vasseur@min.uni-muenchen.de*

[2] *Earth, Ocean and Ecological Sciences, University of Liverpool, Liverpool, United Kingdom*

Accepted 2015 December 22. Received 2015 December 9; in original form 2015 September 24

SUMMARY

The elastic properties of homogeneous, isotropic materials are well constrained. However, in heterogeneous and evolving materials, these essential properties are less well-explored. During sintering of volcanic ash particles by viscous processes as well as during compaction and cementation of sediments, microstructure and porosity undergo changes that affect bulk dynamic elastic properties. Here using a model system of glass particles as an analogue for initially granular rock-forming materials, we have determined porosity and *P*-wave velocity during densification. Using these results, we test models for the kinetics of densification and the resultant evolution of the elastic properties to derive a quantitative description of the coupling between the kinetics of isotropic densification and the evolving dynamic elastic moduli. We demonstrate the power of the resultant model on a wide range of data for non-coherent sediments as well as sedimentary and volcanic rocks. We propose that such constraints be viewed as an essential ingredient of time-dependent models for the deformation of evolving materials in volcanoes and sedimentary basins.

Key words: Probability distributions; Microstructures; Permeability and porosity; Body waves; Acoustic properties; Experimental volcanism.

1 INTRODUCTION

Granular, rock-forming materials are abundant in the Earth system. They represent an essential material state during diagenesis in sedimentary rocks and sintering in volcaniclastics. In such depositional settings, granular materials undergo densification either by viscous 'welding' processes (Quane *et al*. 2009; Vasseur *et al*. 2013; Wadsworth *et al*. 2014; Heap *et al*. 2015; Lavallée *et al*. 2015) or by compaction and cementation (Bourbie & Zinszner 1985; Blair *et al*. 1993; Worden & Burley 2003). During densification, these materials are subjected to stresses, be they tectonic, volcanic or even solely local in nature, yielding deformation and seismicity (Hacker 1997). As such, knowledge of elastic properties of these materials during densification is critical for quantitatively addressing aspects of both deformation and seismicity.

Despite significant advances in our understanding of statistically randomly organized heterogeneous materials (Torquato 2013) and the related scaling laws and bounds for effective elastic properties (Voigt 1928; Reuss 1929; Wyllie *et al*. 1956; Hashin & Shtrikman 1963; Watt *et al*. 1976; Berryman 1980a,b; Quintanilla & Torquato 1995), such constraints remain sparsely tested against experimental data relevant to geological problems. Furthermore, sample microstructure is rarely considered explicitly and rigorously (Eshelby 1957; Wu 1966). Here we test a recent model developed for ideal, randomly generated simulated spherical cavities in homogeneous media (Torquato 2013) against our experimental data across the granular to non-granular transition during densification to elucidate the scaling of elastic properties in heterogeneous media. This study presents the first integration of densification kinetics with a law for evolving elastic moduli, which we anticipate will prove essential in future models of rock formation in sediments and volcaniclastics.

2 MATERIALS AND METHODS

In selecting good analogues for rock-forming materials, we follow the rationale of Blair *et al*. (1993) and Wadsworth *et al*. (2014) who suggested that sintered glass beads represent a uniquely well-characterized analogue system for the constraint of many structural processes in sandstones and volcanic tuffs, respectively. Indeed, Wadsworth *et al*. (2014) showed that effective scaling of the liquid viscosity μ_0 above the glass transition interval T_g and the particle size distribution is sufficient to justify the use of synthetic glass as an analogue for volcanic pyroclasts. They represent a state and material properties that are well known. The caveat to using good glass formers is that they do not capture the complex effects of crystallization and degassing, variable intraclast porosity or cement, all of which may be additional factors to consider in natural systems. Nevertheless, the results achieved below indicate that a powerful first step has been made towards our goals.

The soda-lime silicate (SLS) used here is in the form of spherical glass particles (Spheriglass® A-glass microspheres 1922 and 2530, Potters Industries Inc.) and the borosilicate (BS) is in the form of

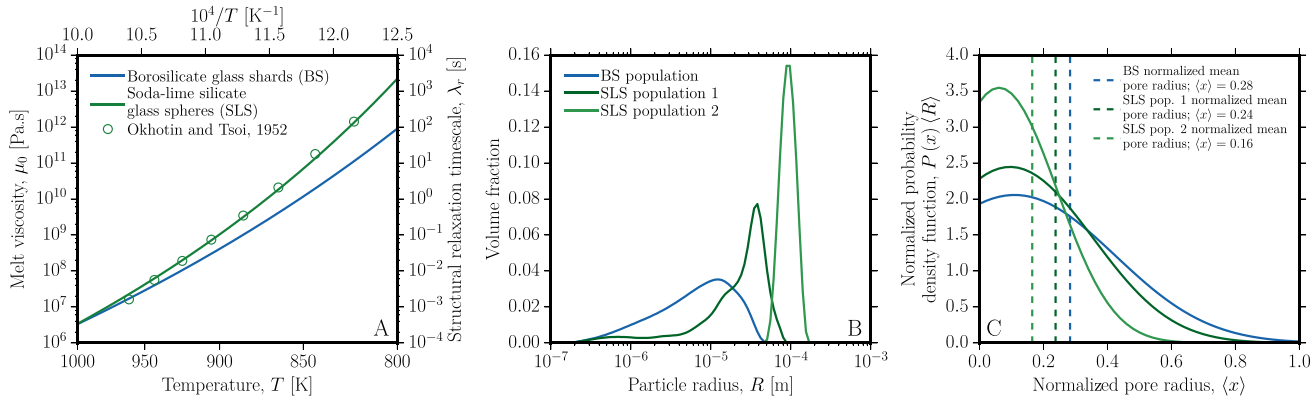

Figure 1. (A) Temperature dependence of the liquid viscosity μ_0 for the two materials used in this study. The Maxwell equivalence between melt viscosity and structural relaxation time λ_r, $\mu_0 = \lambda_r G_\infty$, is given as a computed parameter (second y-axis) using the shear modulus at infinite frequency $G_\infty \approx 10$ GPa (Dingwell & Webb 1990). (B) Particle radius distributions of the granular material sintered herein. (C) Computed probability density functions $P(x)$ related to the calculated pore sizes using eqs (2)–(4) (Lu & Torquato 1992; Torquato 2013).

Table 1. Properties of materials.

Parameter	SLS	BS
A_{VFT}	−2.6387	−2.5602
B_{VFT}	4303.36	4852.2
C_{VFT}	530.754	465.762
ρ_g (kg m^{-3})	2500	2375

glass shard particles (Standard Reference Material 717a, National Institute of Standards and Technology). For these materials, the temperature dependence of the liquid viscosity and the rate-dependent position of the glass transition interval are well constrained (Vasseur *et al*. 2013; Wadsworth *et al*. 2014). We provide the parametrization of the liquid viscosity μ_0 in the form of a Vogel–Fulcher–Tammann expression (Table 1) valid for the experimental range of temperatures (Fig. 1A). The particle radii R are measured using a Coulter laser particle size analyser with a measuring range 0.375–2000 μm (Fig. 1B). The glass densities ρ_g are 2375 and 2500 kg m^{-3} for the BS and SLS materials, respectively (Table 1).

The glass particles were poured in cylindrical ∼97 wt.% alumina crucibles with ∼44 mm inner diameter and 60 mm inner height with a simple loose packing. The sample mass, glass density and crucible geometry constrain the initial pore volume fraction between the particles prior to experimentation (Fig. 1C). The samples were heated in a box furnace 10 K min^{-1} to temperatures of ∼843, 888, 898 and 908 K and held for times between 0 and 32 hr before cooling at a slower rate of ∼5 K min^{-1}. The maximum gradient of temperature recorded in the furnace was ∼40 K m^{-1}, permitting the computation of maximum errors on the liquid viscosity estimation over the sample lengthscale (Fig. 2). The samples were then cored from the crucibles to cylinders of 50 mm height and 25 mm diameter. Their porosities were constrained using helium pycnometry in a Micromeritics Accupyc 1330 device. The microstructures were constrained using micrographs collected on polished sections of subsamples in a scanning electron microscope (Fig. 3).

Following high temperature sintering, the ultrasonic P-wave velocity v_p was measured using a 900 V, 1.5 kHz pulse generated by a JSR DPR300 35 MHz ultrasonic pulser/receiver connected to piezoelectric transducers with a Rhode und Schwarz RTM-1054 500 MHz oscilloscope. The P-wave modulus was then calculated as $M = \rho {v_p}^2$ where ρ is the bulk sample density.

3 EXPERIMENTAL RESULTS

In the following, where we refer to porosity we use bulk porosity to mean total gas volume fraction, as classically defined. We find that at temperatures in excess of the glass transition interval, particles of liquid silicate (droplets) sinter rapidly and nonlinearly under the conditions used here. This is manifest as a bulk reduction in the porosity of a packing of glass particles (Fig. 2). This nonlinearity is dependent on the experimental temperature (via the temperature dependence of the liquid viscosity; Fig. 1(A); see also Vasseur *et al*. 2013) and the particle size distribution (Fig. 1B). The particle-size dependence is clearly evident in the form of a difference in porosity decay rates between SLS population 1 and SLS population 2 despite their identical composition and experimental temperature. The microstructure evolves during this sintering process from granular to non-granular. The end-state is characterized by individual pores that relax to spherical upon isolation (Fig. 3). The P-wave modulus M increases upon densification (Fig. 4). The dependence of M on porosity is seemingly linear below a particular value (see Section 5).

4 VISCOUS SINTERING KINETICS

Viscous sintering involves the flow of liquid into the pore-space between particles, resulting in the bulk density increase and consequent bulk porosity decrease. When the principal stress driving fluid flow is the surface tension of the liquid–vapour interfaces (i.e. when surface tension forces exceed gravitational forces), the sintering process is very well constrained (e.g. Vasseur *et al*. 2013; Wadsworth *et al*. 2014). Explicitly, fluid flow is driven by the Laplace pressure, which for spherical pores is $P_L = 2\Gamma/a$, where Γ is the surface tension value and a is the pore radius. The universal metric for sintering is the bulk density relative to the liquid density, or equivalently, the porosity ϕ. The sintering process in the absence of external stresses has been explicitly modelled in terms of a sintering timescale $\lambda = \mu_0 a/\Gamma$ (Mackenzie & Shuttleworth 1949; Oldroyd 1953). However, an alternative useful approximation of this process is exponentially dependent on the initial porosity ϕ_i such that

$$\phi = \phi_i \exp\left(-\frac{3\Gamma}{2\mu_0 a}t\right) = \phi_i \exp\left(-\frac{3}{2\lambda}t\right). \quad (1)$$

If we make the additional approximation that a is a constant value equivalent to the initial value, then we negate the need to know how a

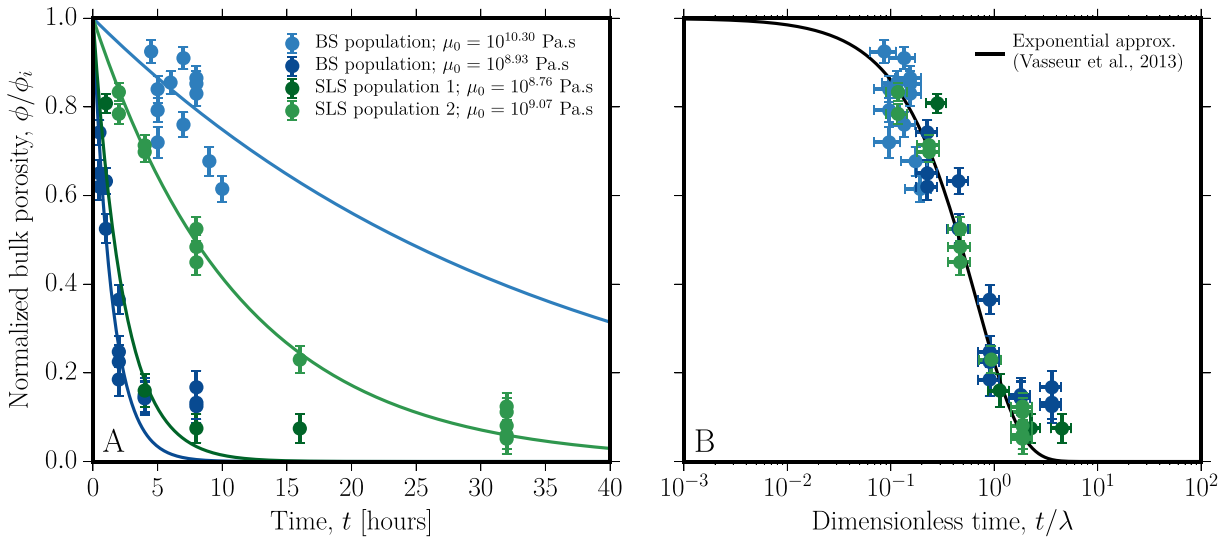

Figure 2. Experimental and model results for viscous sintering experiments. (A,B) The liquid viscosities μ_0 listed are equivalent to experimental temperatures (see Fig. 1). The viscous sintering model (solid curves) is given by eq. (1) (Vasseur *et al*. 2013) and the normalization timescale λ uses the lengthscale predicted for the pores interstitial to the particles by eqs (2)–(4) (see the text).

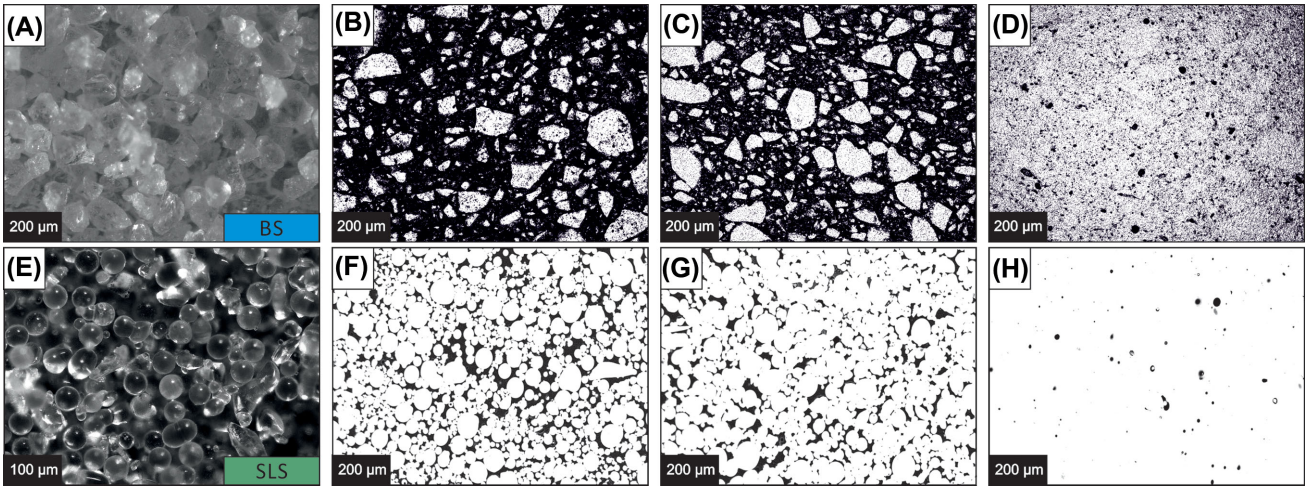

Figure 3. Microstructures of granular material densification by sintering for (A–D) the borosilicate glass shards and (E–H) the soda-lime silicate glass spheres. All images are taken using an optical microscope with plane polarized light and then converted to binary images using the peaks of the grey-scale values as threshold limits other than the first image in panels (A) and (E), which are as-taken. In panels (B–D) and (F–H), the black colour represents the pore phase while the white colour represents the glass.

evolves with ϕ. Vasseur *et al*. (2013) used this approach when fitting for a characteristic sintering lengthscale in place of a because the pore radius is not easily measured. However, a better constraint on a can be obtained from knowledge of R using statistical methods developed for isotropic random heterogeneous particle populations (Torquato 2013). This approach is based on statistical methods and involves the constraint of a probability density function $P(x)$ and its associated cumulative function $F(x)$ where $x = a/R$ and R is the particle radius

$$P(x) = \frac{h_V(x)}{\phi}$$
$$F(x) = \frac{e_V(x)}{\phi}, \qquad (2)$$

where $h_V(x)$ and $e_V(x)$ are the polydisperse void nearest-neighbour probability density function and the associated dimensionless exclusion probability, respectively. If we introduce $\theta = (1 + x)/2$, we have (Lu & Torquato 1992)

$$h_V(x) = \frac{S(1-\phi)}{\langle R\rangle}\left(3y_0\theta^2 + 2y_1\theta + y_2\right)e_V(x)$$
$$e_V(x) = \phi\exp\left(2S(\phi-1)\left(y_0\theta^3 + y_1\theta^2 + y_2\theta\right)\right) \qquad (3)$$

for which S is related to the nth moment of the particle-size distribution $\langle R^n\rangle$ by $S = \langle R^2\rangle\langle R\rangle/\langle R^3\rangle$ and

$$y_0 = \frac{4\phi\langle R\rangle^2\left(\phi + 3S(1-\phi)\right)/\langle R^2\rangle + 8\left(S(1-\phi)\right)^2}{\phi^3}$$
$$y_1 = \frac{6\phi\langle R\rangle^2/\langle R^2\rangle + 9S(1-\phi)}{\phi^2}$$
$$y_2 = \frac{3}{\phi}. \qquad (4)$$

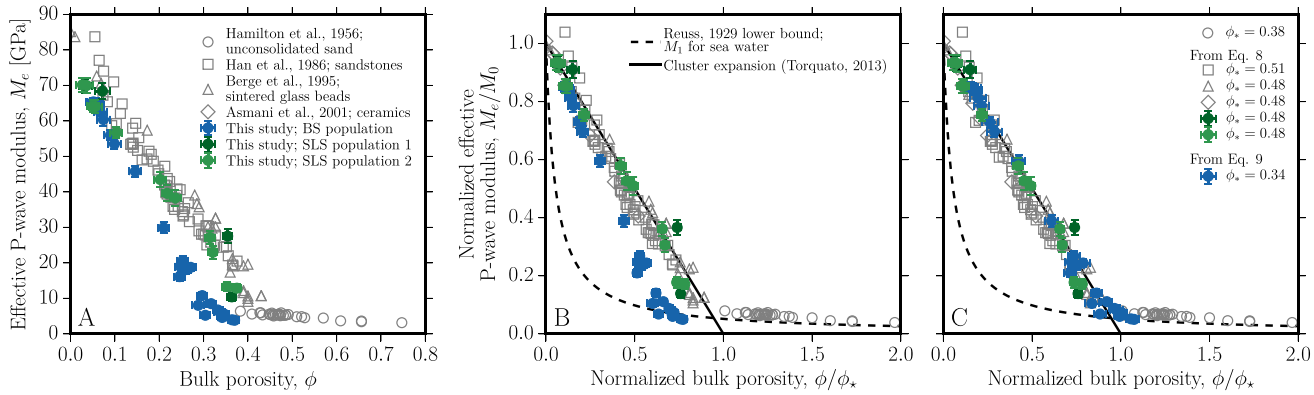

Figure 4. Experimental and model results for the effective *P*-wave modulus M_e. (A) The evolution of M_e with bulk porosity for literature data using unconsolidated sand (Hamilton *et al*. 1956), sandstones (Han *et al*. 1986), sintered glass beads (Berge *et al*. 1995) and sintered alumina ceramics (Asmani *et al*. 2001) for comparison with the SLS and BS data using constraints on the bulk and shear modulus of the glass phase quoted in the text. (B) The data when M_e is normalized by M_0 and ϕ is normalized using ϕ_* predicted by the model of Torquato (2013); eq. (8). (C) The data are treated as in panel (B) but with the use of an empirical ϕ_* (eq. 9) for the BS polydisperse data. In panels (B) and (C), we additionally show the Reuss (1929) lower bound for the case when the pore fluid is sea water, as in the data from Hamilton *et al*. (1956).

In order to go from $P(x)$ to the nth moment of the distribution of x, we integrate using $\langle x^n \rangle = \int_0^\infty x^n P(x)\,\mathrm{d}x$ and a mean value of the pore radius (i.e. $n = 1$) is $\langle a \rangle = \langle x \rangle \langle R \rangle$ (Fig. 1C).

This constraint of a can be used in eq. (1) to predict the sintering kinetics. Upon normalization of ϕ using ϕ_i and t using λ, we find a non-dimensional agreement across all experiments when the a in λ is taken to be $\langle a \rangle$ using eqs (2)–(4) (Fig. 2B). We note that compositional and particle-size differences are accounted for by this normalization method and no fitting parameters are used. While this solution is an approximation of the process and not an explicit description because $\langle a \rangle$ is not taken to be a function of time, it does fit most sintering data to within 95 per cent confidence limits.

5 DYNAMIC ELASTIC MODULI

5.1 Empirical and theoretical models

The *P*-wave modulus M is a dynamic elastic modulus. As such, it can be related to other dynamic moduli, for example, the dynamic bulk modulus K and the dynamic shear modulus G by $M = K + 4G/3$ (Guéguen & Palciauskas 1994). This equivalence provides us with flexibility in applying existing models for K and G adapted for comparison with measurement of M. To do this, we use the well-known $K = M(1+\nu)/3(1-\nu)$ and $G = M(1-2\nu)/2(1-\nu)$ where ν is Poisson's ratio and taken to be 0.238 for all glass materials used here because of their similar composition (Berge *et al*. 1995). Of interest in this work is the dependence of these moduli on the bulk porosity ϕ such that M_0, K_0 and G_0 are defined as the values of the dynamic moduli at $\phi = 0$, that is, those of the solid phase. We work on the widely held assumption that interrelations between dynamic elastic moduli for homogeneous isotropic linear elastic materials can be used to scale those of the effective dynamic elastic moduli (Torquato 2013).

First, we note that the evolution of M with ϕ appears to be linear over the range of ϕ achieved here (Fig. 4A; see also Vasseur *et al*. 2013) and simple linear regression through the data of the form $M = M_0 - k\phi$ yields fitted values of M_0 of 77.7 and 75.14 GPa for the BS and SLS compositions, respectively. No measureable difference is observed between the two SLS populations used. Employing the equivalences proposed above, this would yield calculated values of dynamic K_0 and G_0 of 42.08 and 26.72 GPa for the BS composition and 40.69 and 25.84 GPa for the SLS composition, respectively. Additionally, this empirical linear approach would yield a ϕ intercept at $M = 0$, termed ϕ_*, of 0.36 and 0.46, for the BS and SLS, respectively. The ϕ_* reduces to 0.34 for the BS population when the nonlinear deviation at high $\phi > 0.3$ is disregarded. Vasseur *et al*. (2013) have proposed that this nonlinear deviation is due to the onset of a granular system prior to significant sintering. However, while this empirical linear regression provides excellent agreement with the data, it is less satisfying than a theoretical approach.

Numerous empirical and theoretical lower and upper bounds, as well as exact solutions for the elastic moduli of composite materials, have been derived for idealized systems (Table 2). Here we introduce these models for the case of two-phase suspensions of pores in turn and test their power in describing both our data sets and data sets from the literature for composite synthetic and natural systems. Fig. 5 summarizes all the models listed hereafter.

First and most simply, the Voigt (1928) upper bound is the basic threshold, which states that $M_e \leq M_0(1-\phi) + M_1\phi$ where M_e and M_1 are the effective modulus of the porous medium and the modulus of the fluid phase occupying the pores, respectively (Fig. 5). The second term vanishes when the pore fluid is of negligible modulus. Similarly, the Reuss (1929) lower bound states that $M_e \geq ((1-\phi)/M_0 + \phi/M_1)^{-1}$, which vanishes when the pore fluid is of negligible modulus (Fig. 5). Both the Voigt upper bound and the Reuss lower bound imply that at $\phi = 0$, $M = M_0$ and at $\phi = 1$, $M = M_1$. In the case of the Voigt bound it is inconsequential if $M_1 \approx 0$. Table 2 gives these bounds in their general form for multiphase composite materials. These empirical bounds do not explicitly match most data for porous systems (Berge *et al*. 1995). Improvements can be made when the upper and lower bounds are derived from a theoretical basis.

The first of these categories of theoretical bounds is given by the seminal work of Hashin–Shtrikman (Hashin 1962; Hashin & Shtrikman 1963). These upper bounds on the effective bulk and shear modulus K_e and G_e are given by

$$K_e \leq K_0 + \frac{\phi}{(K_1 - K_0)^{-1} + \alpha_{\mathrm{HS}}(1-\phi)}$$
$$G_e \leq G_0 + \frac{\phi}{(G_1 - G_0)^{-1} + \beta_{\mathrm{HS}}(1-\phi)}, \qquad (5)$$

Table 2. Empirical and theoretical bounds and models.

Reference	Modulus[a]
Upper bound (Voigt 1928)	$M_e \leq \sum_{i=0}^{N} f_i M_i$
Lower bound (Reuss 1929)	$M_e \geq \left(\sum_{i=0}^{N} \frac{f_i}{M_i} \right)^{-1}$
Upper bound (Hashin & Shtrikman 1963)	$K_e \leq K_0 + \frac{f_1}{(K_1 - K_0)^{-1} + \alpha_{\mathrm{HS}} f_0}$
	$G_e \leq G_0 + \frac{f_1}{(G_1 - G_0)^{-1} + \beta_{\mathrm{HS}} f_0}$
Lower bound (Hashin & Shtrikman 1963)	$K_e \geq K_1 + \frac{f_0}{(K_0 - K_1)^{-1} + \alpha_{\mathrm{HS}} f_1}$
	$G_e \geq G_1 + \frac{f_0}{(G_0 - G_1)^{-1} + \beta_{\mathrm{HS}} f_1}$
Self-consistent approximation (Berryman 1980a)	$\sum_{i=0}^{N} \alpha_{\mathrm{SCi}} f_i (K_i - K_e) = 0$
	$\sum_{i=0}^{N} \beta_{\mathrm{SCi}} f_i (G_i - G_e) = 0$
Cluster expansion method (Torquato 2013)	$K_e = K_0 \left(1 + f_1 (K_1 - K_0) \left(\frac{1+\alpha_T}{K_1 + \alpha_T K_0} \right) \right) + \mathcal{O}(f_1^2)$
	$G_e = G_0 \left(1 + f_1 (G_1 - G_0) \left(\frac{1+\beta_T}{G_1 + \beta_T G_0} \right) \right) + \mathcal{O}(f_1^2)$

[a] f_i is the volume fraction of the ith phase, and α_{SCi} and β_{SCi} are the microstructure-dependent parameters of the ith phase defined in Table 3.

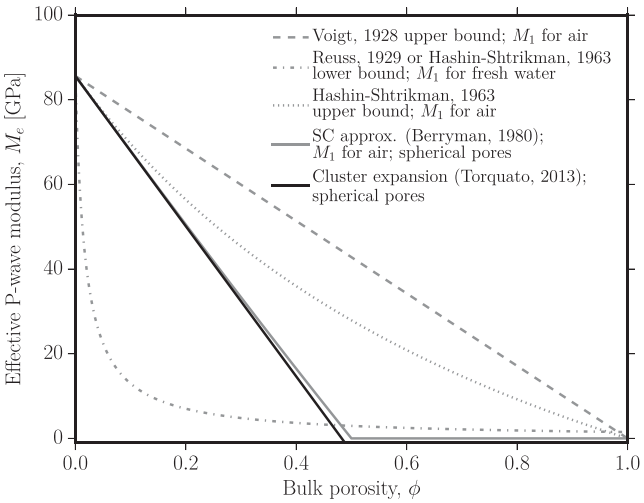

Figure 5. Bounds and solutions of the effective dynamic modulus (here cast as the P-wave modulus M_e) as a function of the system porosity ϕ. For illustrative purpose in this figure only, we consistently use $M_0 = 85.16$ GPa (Berge *et al*. 1995). See the text and Table 2 for details.

where $\alpha_{\mathrm{HS}} = (K_0 + 4G_0/3)^{-1}$ and $\beta_{\mathrm{HS}} = 2(K_0 + 2G_0)/5G_0(K_0 + 4G_0/3)$ (Fig. 5). The lower bounds vanish (i.e. $K_e \approx 0$ and $G_e \approx 0$) when the pore fluid is air because it is of negligible moduli. The solution for when the pore fluid is not air is discussed in the derivation by Hashin & Shtrikman (1963). Similarly, it reduces to the Reuss (1929) lower bound when the pore fluid is water because its shear modulus is negligible in the relaxed state. Table 2 gives these bounds in their general form for two-phase composite materials.

An effective medium approach, the self-consistent (SC) approximation, yields a system of two coupled equations which must be solved numerically by simultaneous iteration. These are (Berryman 1980a,b; Berryman 1995)

$$\begin{aligned} \alpha_{\mathrm{SC0}}(1-\phi)(K_0 - K_e) + \alpha_{\mathrm{SC1}}\phi(K_1 - K_e) &= 0 \\ \beta_{\mathrm{SC0}}(1-\phi)(G_0 - G_e) + \beta_{\mathrm{SC1}}\phi(G_1 - G_e) &= 0 \end{aligned} \tag{6}$$

where $\alpha_{\mathrm{SC1}}, \alpha_{\mathrm{SC0}}, \beta_{\mathrm{SC1}}$ and β_{SC0} represent microstructure-dependent parameters and the subscripts SC0 and SC1 refer to the solid and fluid phases, respectively (Fig. 5). Constraints of the microstructurally defined solutions for these shape-dependent parameters used in eq. (6) exist for some simple geometries (Table 3). Table 2 gives these coupled equations in their general form for multiphase composite materials.

Finally, an explicit prediction for the effective dynamic bulk and shear moduli can be found by a cluster expansion method for a dilute dispersion of spherical cavities in an otherwise homogeneous medium as (Torquato 2013)

$$\begin{aligned} K_e &= K_0 \left(1 - \phi \left(1 + \alpha_T^{-1}\right)\right) + \mathcal{O}\left(\phi^2\right) \\ G_e &= G_0 \left(1 - \phi \left(1 + \beta_T^{-1}\right)\right) + \mathcal{O}\left(\phi^2\right), \end{aligned} \tag{7}$$

where $\alpha_T = 4G_0/3K_0$ and $\beta_T = (9K_0 + 8G_0)/(6K_0 + 12G_0)$ (Fig. 5). Table 2 gives these equations in their general form for two-phase composite materials. Combination of the interrelation between M, K and G given earlier and eq. (7) yields

$$M_e = M_0 - \phi \left(K_0 \left(1 + \alpha_T^{-1}\right) + \frac{4}{3} G_0 \left(1 + \beta_T^{-1}\right) \right). \tag{8}$$

The intercept of this model at a value of $M_e = 0$ occurs at $\phi_* = M_0/(K_0(1 + \alpha_T^{-1}) + 4G_0(1 + \beta_T^{-1})/3)$. ϕ_* and M_0 therefore provide normalization parameters for ϕ and M_e so that different data sets may be compared. This is akin to generalizing eq. (8) such that

$$M_e = M_0 \left(1 - \frac{\phi}{\phi_*}\right), \tag{9}$$

where ϕ_* is given as arranged from eq. (8) or could be empirically defined after Mavko & Mukerji (1998).

5.2 Model reliability assessment

We start by assessing published data for M_e as a function of ϕ also constrained using unconsolidated sediments in sea water (Hamilton *et al*. 1956), sandstones (Han *et al*. 1986), sintered soda-lime silica glass beads (Berge *et al*. 1995) and sintered ceramics (Asmani *et al*.

Table 3. Self-consistent microstructure-dependent parameters.

Shape	α_{SCi}[a]	β_{SCi}[a]
Sphere	$\frac{K_e+4G_e/3}{K_i+4G_e/3}$	$\frac{G_e+\xi}{G_i+\xi}$
Needle	$\frac{K_e+G_e+G_i/3}{K_i+G_e+G_i/3}$	$\frac{1}{5}\left(\frac{4G_e}{G_e+G_i}+\frac{2(G_e+\chi)}{G_i+\chi}+\frac{K_i+4G_e/3}{K_i+G_e+G_i/3}\right)$
Penny crack	$\frac{K_e+4G_i/3}{K_i+4G_i/3+\pi r_p\psi}$	$\frac{1}{5}\left(1+\frac{8G_e}{4G_i+\pi r_p(G_e+2\psi)}+\frac{2(K_i+2(G_i+G_e)/3)}{K_i+4G_i/3+\pi r_p\psi}\right)$

[a] $\xi=\frac{G_e(9K_e+8G_e)}{6K_e+12G_e}$, $\chi=\frac{G_e(3K_e+G_e)}{3K_e+7G_e}$, $\psi=\frac{G_e(3K_e+G_e)}{3K_e+4G_e}$ and r_p is the aspect ratio of the cracks.

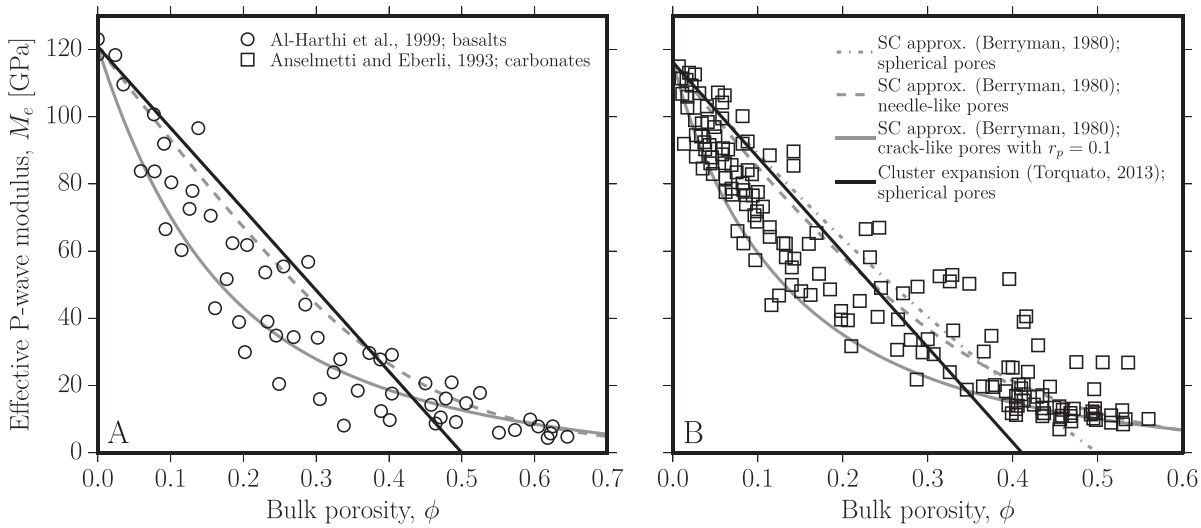

Figure 6. Experimental and model constraints for the effective *P*-wave modulus M_e as a function of the sample porosity ϕ for (A) basalts (Al-Harthi *et al*. 1999) and (B) carbonates (Anselmetti & Eberli 1993). The predictions from eq. (8) (Torquato 2013) and eq. (6) (self-consistent approximation; Berryman 1980a) are included where eq. (6) is varied for different pore geometries (see Table 3). The Voigt (1928), Reuss (1929) and Hashin & Shtrikman (1963) bounds are omitted for clarity as they do not provide a good description of these data.

2001). For the data from Han *et al*. (1986), we apply the published correction (Gal *et al*. 1999) when the clay content influences the results prior to plotting here and to do this we use their suggested clay porosity of 0.4. For the composition used by Berge *et al*. (1995), $K_0 = 46.1 \pm 0.7$ GPa and $G_0 = 29.2 \pm 0.4$ GPa, which is in reasonable agreement with the values of the compositionally similar SLS populations described above. The M_0 computed from v_p and ρ for the Berge *et al*. (1995) spheres is therefore 85.03 GPa. Use of eq. (8) with both the data of Berge *et al*. (1995) and the data from this study for the SLS spheres results in excellent agreement with input only of M_0 and results in the facility to compute any dynamic elastic modulus from these data for $\phi \leq \phi_*$ (Fig. 4). Additionally, the extrapolation of eq. (8) to $M_e = 0$ yields ϕ_* values in good agreement with the empirical values from linear regression analysis such that upon normalization all data for initially spherical sintered glass beads collapse onto a single linear description (Fig. 4B). We note, however, that the BS population of non-equant fragments does not agree well with the data for spherical particles.

It is explicit in the analysis of Torquato (2013) that eqs (7)–(8) are most appropriate for a monodisperse suspension of cavities in a homogeneous medium. It is interesting to note, therefore, that the evolution of M_e for densifying spherical particles (with initially highly non-spherical interstitial pores; Fig. 3), provides excellent agreement with eq. (8) (Fig. 4). We also note that if the value of ϕ_* for the BS data is permitted to be the empirically defined value from linear regression analysis, then we find that, upon normalization, they also agree very well with the prediction of eq. (8) (Fig. 4C). This is identical to using eq. (9) with a fitted ϕ_*, similar to the method of Mavko & Mukerji (1998). We therefore conclude that for these granular to non-granular systems, the threshold porosity at which the system undergoes a transition from granular to cohesive represents a porosity at which the conductance of a *P*-wave becomes linearly dependent on the porosity (e.g. Nur *et al*. 1991; Nur *et al*. 1998). This critical porosity, here termed ϕ_*, would therefore be proportional to a loose random packing in the granular state at which the system gains the ability to bear a significant load (i.e. rigidity) and, in turn, would be able to be related to the dispersivity of the initial particle size. However, solutions for such a packing porosity threshold remain elusive (Torquato 2013).

Mavko & Mukerji (1998) and Nur *et al*. (1998) employ an analysis that relies on an empirically determined ϕ_*. In the data for sandstones, we find that $\phi_* = 0.51$ when we use eq. (8). Similarly, we find $\phi_* = 0.48$ for all sintered glass beads and ceramics data when we use eq. (8). These values are slightly higher than the $\phi_* \approx 0.4$ found by Nur *et al*. (1998) for sandstones and sintered glass beads using the same literature data (Han *et al*. 1986; Berge *et al*. 1995) and a simpler linear regression analysis.

We find excellent agreement in these simple systems such that eq. (8) (Torquato 2013) seemingly provides the best description of the data when ϕ_* is directly predicted by the model (e.g. for the SLS, Han *et al*. (1986), Berge *et al*. (1995) and Asmani *et al*. (2001) data) or permitted to be empirically defined (e.g. for the BS data). Interestingly, both the most poorly sintered BS population and the unconsolidated sand (Hamilton *et al*. 1956) are well described by the Reuss (1929) lower bound above ϕ_*.

The dynamic elastic modulus of other natural rocks, such as that for basalts (Al-Harthi *et al*. 1999) and carbonates (Anselmetti & Eberli 1993), can also be scaled in the way described above (Fig. 6).

However, simple scaling or description appears unsatisfactory in describing these data and the definition of a value of ϕ_* appears unreasonable. Therefore, we suggest that in such a case it may be reasonable (until further constraints are available) to use the self-consistent approximation, eq. (6), with various definitions of the shape-parameters (Table 3). It is clear that for the elastic moduli of these heterogeneous natural systems, more rigorous microstructural details are required to assess the efficacy of these models upon normalization. A final detail pertinent to natural rocks is the propensity for cementation processes (in sedimentary systems) or pore-infilling alteration (i.e. in volcanic systems) to modify the solid medium. A particular case is when cement is allochthonous or, as Gal *et al*. (1999) found, when intrapore clay influences the *P*-wave velocities. This is a significant problem for extension of theoretical constraint to natural systems and requires substantial further work.

6 CONCLUSIONS

The viscous sintering kinetics of glass beads is scaled to a single description over a wide range of initial particle size distributions, compositions and temperatures. These isotropic materials, often considered a good analogue for many rock-forming systems from sandstones to volcanic tuffs, are increasingly microstructurally homogeneous as densification proceeds. We find that constraining the density, the *P*-wave velocity and one further elastic parameter of a solid phase is sufficient to model the evolution of the *P*-wave velocity as a function of porosity in a suspension or dispersion up to a threshold porosity at which the system is entirely granular. The use of the cluster expansion model here represents a significant improvement on existing empirical scaling. We find excellent agreement between our measurements and theoretical considerations without the necessity for fitting which allows all dynamic elastic moduli to be derived. Finally, comparison with less well-constrained data for other systems of rock-forming and ceramic media validates a near-universal scaling for the elastic moduli of isotropic rocks of which glass-hosted volcanic pyroclasts are a prominent example. A further advance tackling the complexity of some natural systems for which the isotropic assumption may fail will require more theoretical work.

ACKNOWLEDGEMENTS

We acknowledge funding from the EU-funded FP7 under grant agreement No. 282759 (VUELCO) and the European Research Council (ERC) for the Advanced Grant on Experimental Volcanology in the Earth System (EVOKES, No. 247076) and the Starting Grant on Strain Localisation in Magma (SLiM, No. 306488). We thank Michael J. Heap for reviewing the manuscript.

REFERENCES

Al-Harthi, A.A., Al-Amri, R.M. & Shehata, W.M., 1999. The porosity and engineering properties of vesicular basalt in Saudi Arabia, *Eng. Geol.,* **54**(3), 313–320.

Anselmetti, F.S. & Eberli, G.P., 1993. Controls on sonic velocity in carbonates, *Pure appl. Geophys.,* **141**(2–4), 287–323.

Asmani, M., Kermel, C., Leriche, A. & Ourak, M., 2001. Influence of porosity on Young's modulus and Poisson's ratio in alumina ceramics, *J. Eur. Ceram. Soc.,* **21**(8), 1081–1086.

Berge, P.A., Bonner, B.P. & Berryman, J.G., 1995. Ultrasonic velocity-porosity relationships for sandstone analogs made from fused glass beads, *Geophysics,* **60**(1), 108–119.

Berryman, J.G., 1980a. Long-wavelength propagation in composite elastic media I. Spherical inclusions, *J. acoust. Soc. Am.,* **68**(6), 1809–1819.

Berryman, J.G., 1980b. Long-wavelength propagation in composite elastic media II. Ellipsoidal inclusions, *J. acoust. Soc. Am.,* **68**(6), 1820–1831.

Berryman, J.G., 1995. Mixture theories for rock properties, in *Rock Physics and Phase Relations: A Handbook of Physical Constants,* Vol. 3, pp. 205–228, American Geophysical Union Online Reference Shelf.

Blair, S.C., Berge, P.A. & Berryman, J.G., 1993. *Two-Point Correlation Functions to Characterize Microgeometry and Estimate Permeabilities of Synthetic and Natural Sandstones,* Lawrence Livermore National Lab.

Bourbie, T. & Zinszner, B., 1985. Hydraulic and acoustic properties as a function of porosity in Fontainebleau sandstone, *J. geophys. Res.,* **90**(B13), 11 524–11 532.

Dingwell, D.B. & Webb, S.L., 1990. Relaxation in silicate melts, *Eur. J. Mineral.,* **2**(4), 427–449.

Eshelby, J.D., 1957. The determination of the elastic field of an ellipsoidal inclusion, and related problems, *Proc. R. Soc. A,* **241**(1226), 376–396.

Gal, D., Dvorkin, J. & Nur, A., 1999. Elastic-wave velocities in sandstones with non-load-bearing clay, *Geophys. Res. Lett.,* **26**(7), 939–942.

Guéguen, Y. & Palciauskas, V., 1994. *Introduction to the Physics of Rocks,* Princeton Univ. Press.

Hacker, B., 1997. Diagenesis and fault valve seismicity of crustal faults, *J. geophys. Res.,* **102**(B11), 24 459–24 467.

Hamilton, E.L., Shumway, G., Menard, H.W. & Shipek, C.J., 1956. Acoustic and other physical properties of shallow-water sediments off San Diego, *J. acoust. Soc. Am.,* **28**(1), 1007–1022.

Han, D.-H., Nur, A. & Morgan, D., 1986. Effects of porosity and clay content on wave velocities in sandstones, *Geophysics,* **51**(11), 2093–2107.

Hashin, Z., 1962. The elastic moduli of heterogeneous materials, *J. appl. Mech.,* **29**(1), 143–150.

Hashin, Z. & Shtrikman, S., 1963. A variational approach to the theory of the elastic behaviour of multiphase materials, *J. Mech. Phys. Solids,* **11**(2), 127–140.

Heap, M.J., Farquharson, J.I., Wadsworth, F.B., Kolzenburg, S. & Russell, J.K., 2015. Timescales for permeability reduction and strength recovery in densifying magma, *Earth planet. Sci. Lett.,* **429,** 223–233.

Lavallée, Y. *et al.*, 2015. Eruption and emplacement timescales of ignimbrite super-eruptions from thermo-kinetics of glass shards, *Front. Earth Sci.,* **3**(2), doi:10.3389/feart.2015.00002.

Lu, B. & Torquato, S., 1992. Nearest-surface distribution functions for polydispersed particle systems, *Phys. Rev. A,* **45**(8), 5530–5544.

Mackenzie, J.K. & Shuttleworth, R., 1949. A phenomenological theory of sintering, *Proc. Phys. Soc. B,* **62**(12), 833–852.

Mavko, G. & Mukerji, T., 1998. Comparison of the Krief and critical porosity models for prediction of porosity and Vp/Vs, *Geophysics,* **63**(3), 925–927.

Nur, A., Marion, D. & Yin, H., 1991. Wave velocities in sediments, in *Shear Waves in Marine Sediments,* pp. 131–140, eds Hovem, J., Richardson, M. & Stoll, R., Springer.

Nur, A., Mavko, G., Dvorkin, J. & Galmudi, D., 1998. Critical porosity: a key to relating physical properties to porosity in rocks, *Leading Edge,* **17**(3), 357–362.

Oldroyd, J.G., 1953. The elastic and viscous properties of emulsions and suspensions, *Proc. R. Soc. A,* **218**(1132), 122–132.

Quane, S.L., Russell, J.K. & Friedlander, E.A., 2009. Time scales of compaction in volcanic systems, *Geology,* **37**(5), 471–474.

Quintanilla, J. & Torquato, S., 1995. New bounds on the elastic moduli of suspensions of spheres, *J. appl. Phys.,* **77**(9), 4361–4372.

Reuss, A., 1929. Berechnung der Fließgrenze von Mischkristallen auf Grund der Plastizitätsbedingung für Einkristalle, *Z. Angew. Math. Mech.,* **9**(1), 49–58.

Torquato, S., 2013. *Random Heterogeneous Materials: Microstructure and Macroscopic Properties,* Springer Science and Business Media.

Vasseur, J., Wadsworth, F.B., Lavallée, Y., Hess, K. & Dingwell, D.B., 2013.

Volcanic sintering: timescales of viscous densification and strength recovery, *Geophys. Res. Lett.,* **40**(21), 5658–5664.

Voigt, W., 1928. *Lehrbuch der Kristallphysik,* Teubner Verlag.

Wadsworth, F.B., Vasseur, J., von Aulock, F.W., Hess, K.-U., Scheu, B., Lavallée, Y. & Dingwell, D.B., 2014. Nonisothermal viscous sintering of volcanic ash, *J. geophys. Res.,* **119**(12), 8792–8804.

Watt, J.P., Davies, G.F. & O'Connell, R.J., 1976. The elastic properties of composite materials, *Rev. Geophys.,* **14**(4), 541–563.

Worden, R.H. & Burley, S.D., 2003. Sandstone diagenesis: the evolution of sand to stone, in *Sandstone Diagenesis: Recent and Ancient,* pp. 3–44, eds Worden, R.H. & Burley, S.D., Blackwell Publishing Ltd.

Wu, T.T., 1966. The effect of inclusion shape on the elastic moduli of a two-phase material, *Int. J. Solids Struct.,* **2**(1), 1–8.

Wyllie, M.R.J., Gregory, A.R. & Gardner, L.W., 1956. Elastic wave velocities in heterogeneous and porous media, *Geophysics,* **21**(1), 41–70.